

Article

# Boosting Blue Self-Trapped Exciton Emission in All-Inorganic Zero-Dimensional Metal Halide Cs<sub>2</sub>ZnCl<sub>4</sub> via Zirconium (IV) Doping

Ye Tian <sup>1</sup>, Qilin Wei <sup>2,\*</sup>, Lian Duan <sup>3</sup> and Chengyu Peng <sup>3,\*</sup>

<sup>1</sup> School of Semiconductors and Physics, North University of China, Taiyuan 030051, China; 20230127@nuc.edu.cn

<sup>2</sup> School of Chemistry and Chemical Engineering, Shandong University, Jinan 250100, China

<sup>3</sup> Traffic Information Engineering Institute, Guangxi Transport Vocational and Technical College, Nanning 530004, China; duanlianxs@foxmail.com

\* Correspondence: qlwei@sdu.edu.cn (Q.W.); chengyu\_peng@126.com (C.P.)

**Abstract:** Low-dimensional metal halides with efficient luminescence properties have received widespread attention recently. However, nontoxic and stable low-dimensional metal halides with efficient blue emission are rarely reported. We used a solvothermal synthesis method to synthesize tetravalent zirconium ion-doped all-inorganic zero-dimensional Cs<sub>2</sub>ZnCl<sub>4</sub> for the first time. Bright blue emission in the range of 370 nm–700 nm with a emission maximum at 456 nm was observed in Zr<sup>4+</sup>:Cs<sub>2</sub>ZnCl<sub>4</sub> accompanied by a large Stokes shift, which was due to self-trapped excitons (STEs) caused by the lattice vibrations of the twisted structure. Simultaneously, the PLQY of Zr<sup>4+</sup>:Cs<sub>2</sub>ZnCl<sub>4</sub> achieve an impressive 89.67%, positioning it as a compelling contender for future applications in blue-light technology.

**Keywords:** low-dimensional metal halides; blue emission; Zr<sup>4+</sup>:Cs<sub>2</sub>ZnCl<sub>4</sub>; self-trapped excitons



**Citation:** Tian, Y.; Wei, Q.; Duan, L.; Peng, C. Boosting Blue Self-Trapped Exciton Emission in All-Inorganic Zero-Dimensional Metal Halide Cs<sub>2</sub>ZnCl<sub>4</sub> via Zirconium (IV) Doping. *Molecules* **2024**, *29*, 1651. <https://doi.org/10.3390/molecules29071651>

Academic Editor: Panwang Zhou

Received: 19 March 2024

Revised: 1 April 2024

Accepted: 2 April 2024

Published: 6 April 2024



**Copyright:** © 2024 by the authors. Licensee MDPI, Basel, Switzerland. This article is an open access article distributed under the terms and conditions of the Creative Commons Attribution (CC BY) license (<https://creativecommons.org/licenses/by/4.0/>).

## 1. Introduction

The broad prospects of solid-state lighting and full-color displays have promoted the rapid development of luminescent materials. Red, green, and blue light sources covering the entire visible light range are required to produce effective white light. The design and manufacture of blue light has proven to be the most challenging of the three sources. For example, blue light-emitting diodes became available two decades after red and green light-emitting diodes were successfully manufactured using epitaxial inorganic technology [1,2].

In the past decade, low-dimensional metal halide luminescent materials have been extensively studied. In particular, zero-dimensional (0D) metal halides have attracted widespread attention due to their high photoluminescence quantum yields (PLQYs) [3]. Various crystal materials including tetrahedral BX<sub>4</sub>, pyramidal BX<sub>5</sub>, and octahedral BX<sub>6</sub> have been reported in metal halides with a 0D structure [4–6]. Green, yellow, and red emission with high PLQY was achieved in 0D metal halides [5,7–10]. However, blue-emitting metal halides with high efficiency and stability remain challenging. Recently, some lead-based low-dimensional metal halides with efficient blue-light emission have been reported [11–13]. Despite the fascinating optical properties of these Pb-based compounds, the toxicity of Pb<sup>2+</sup> hinders their further practical applications. Therefore, it is particularly important to design low-toxic or non-toxic low-dimensional metal halide materials with efficient blue emission properties for future applications. At present, Cu(I)-based compounds with high-efficiency blue emission characteristics are the most representative low-toxic halide materials and have received widespread attention from the scientific community [14–18]. The luminescence of Cu(I)-based low-dimensional metal halides comes from the self-trapped excitons formed by its soft lattice structure. The existence of

organic macromolecules and large-sized inorganic cations enable the production of a strong spatial confinement effect, resulting in photogenerated excitons. These photogenerated excitons are strongly bound within the inorganic polyhedron which then emits photons outward through radiative recombination, finally producing efficient luminescence. However, the naturally unstable and easily oxidized characteristics of Cu(I) are still a problem that needs to be solved urgently. Xia et al. reported a zero-dimensional Sn(IV)-based organic–inorganic hybrid metal halide  $(C_6N_2H_{16}Cl)_2SnCl_6$  [19]. This material exhibited broadband blue-light emission, which came from the self-trapped excitons formed inside the crystal. At the same time,  $(C_6N_2H_{16}Cl)_2SnCl_6$  also had ultra-high stability. The PL intensity of  $(C_6N_2H_{16}Cl)_2SnCl_6$  remained stable for more than three months. Its PL intensity remained at about 50% of the initial intensity when the temperature rose to 450 K. However, the emission efficiency of  $(C_6N_2H_{16}Cl)_2SnCl_6$  was only 8.1%, which is too low for large-scale commercial applications. Through theoretical calculations, they confirmed that the lower PLQY of  $(C_6N_2H_{16}Cl)_2SnCl_6$  was caused by the disappearance of the lone-pair electrons on the  $Sn^{4+}$  cations, which led to the smallest distortion and finally led to the low PLQY. In addition to Sn(IV)-based compounds, In(III)-based compounds have also attracted much attention recently. Saparov et al. reported a new zero-dimensional organic–inorganic hybrid indium bromide  $RInBr_4$  [ $R$  = trimethyl(4-stilbenyl)methylammonium cation] [20]. The  $RInBr_4$  showed bright-blue emission at 437 nm under the 391 nm UV excitation with Commission Internationale de l’Eclairage color coordinates of (0.19, 0.20) and a high photoluminescence quantum yield of 16.36% at room temperature. In addition, this novel hybrid indium bromide demonstrated significantly improved environmental stability. In addition to indium bromide, low-dimensional organic–inorganic hybrid indium chloride with blue-light emission has also been reported. Yue et al. reported two indium chlorides with blue-light emission:  $[H_2EP]_2InCl_6 \cdot Cl \cdot H_2O \cdot C_3H_6O$  and  $[H_3AEP]InCl_6 \cdot H_2O$  ( $EP$  = 1-ethylpiperazine,  $AEP$  = N-aminoethyl piperazine) [21]. The blue emission of both compounds came from self-trapped excitons generated by their soft lattice structures. However, the PLQY of  $[H_2EP]_2InCl_6 \cdot Cl \cdot H_2O \cdot C_3H_6O$  and  $[H_3AEP]InCl_6 \cdot H_2O$  was not high. The highest was only 13.44%, which is far from meeting the needs of practical applications. A series of zero-dimensional In-based halides:  $[H_3AEPz]_2InCl_9 \cdot (H_2O)_2$  ( $AEPz$  = N-aminoethylpiperazine),  $[H_2AMPd]_2InCl_7$  [ $AMPd$  = 4-(aminomethyl)piperidine], and  $[H_2PhPz]_2InCl_7 \cdot (H_2O)_2$  ( $PhPz$  = 1-phenylpiperazine), reported by Lei et al., had a maximum PLQY of no more than 20% [22]. Therefore, In(III)- and Sn(IV)-based materials are still plagued by problems such as low luminous efficiency and poor optical properties, which cannot meet the needs of practical applications [19–22].

In recent years, low-dimensional Zn(II)-based materials based on Zn with a  $d^{10}$  electronic configuration have gradually attracted the attention of researchers due to their variable crystal structure, low toxicity, and high stability properties. Currently, efficient emission is achieved in the all-inorganic zero-dimensional Zn-based compound  $Cs-Zn-X$  ( $X$  = Cl, Br, and I) by doping modification with  $Cu^+$  ions. Through structural transformation and halogen control, the emission color of  $Cs-Zn-X$  can be effectively adjusted from violet to blue [5,15,23,24]. However, these materials still face the problem of poor stability due to the presence of  $Cu^{2+}$  ions. After being left for a period of time, their optical performance will gradually deteriorate due to the oxidation of  $Cu^+$  to  $Cu^{2+}$  until they lose optical activity. The key to solving this problem is whether we can find a stable ion as a dopant and incorporate it into the  $Cs-Zn-X$  crystal lattice so that it can produce efficient and stable blue emissions. We have noticed that the all-inorganic metal halide double perovskite material  $Cs_2ZrCl_6$  has received widespread attention recently, and this material can produce blue-light emission under ultraviolet light excitation [25,26]. Research results show that this blue luminescence comes from STEs generated by the strong electron–phonon coupling effect of the  $[ZrCl_6]^{2-}$  inorganic octahedron in  $Cs_2ZrCl_6$  [26]. Therefore,  $Zr^{4+}$  ions can be incorporated into host materials as optically active ions to achieve blue-light emission.

Herein, we used nontoxic and stable all-inorganic  $Cs_2ZnCl_4$  as the host and  $Zr^{4+}$  ions as the dopant to design a zero-dimensional metal halide  $Zr^{4+}:Cs_2ZnCl_4$  with efficient

blue emission. By introducing  $Zr^{4+}$  into non-luminescent  $Cs_2ZnCl_4$ , efficient blue-light emission ( $\lambda_{em} = 456$  nm under 260 nm UV excitation) was achieved with a PLQY as high as 89.67%. Detailed optical characterization including photoluminescence (PL) decay lifetime and temperature-dependent PL spectra demonstrated that the bright blue emission in  $Zr^{4+}:Cs_2ZnCl_4$  originated from self-trapped exciton (STE) emission. We believe that this work can provide a reference for the future design and synthesis of low-toxic metal halide materials with efficient blue emission properties.

## 2. Results and Discussion

### 2.1. Structure and Morphology

Pure  $Cs_2ZnCl_4$  and  $Zr^{4+}$ -doped  $Cs_2ZnCl_4$  crystal samples were prepared by the solvothermal method using cesium chloride, zinc chloride, and zirconium chloride. Crystallographic data indicated that  $Cs_2ZnCl_4$  belonged to the orthorhombic  $Pnma$  space group and had a typical 0D structure. In each  $[ZnCl_4]^{2-}$  tetrahedron, one  $Zn^{2+}$  ion occupied the central position and four  $Cl^-$  ions were connected to it to form a highly symmetrical tetrahedral geometry, as shown in Figure 1a. Each  $[ZnCl_4]^{2-}$  tetrahedron was distributed in isolation and the distance between two adjacent tetrahedrons was 6.6 Å (calculated based on the  $Zn^{2+}$  ion distance). The tetrahedrons exhibited a typical 0D structure at the molecular level.  $Cs^+$  ions served as a supporting framework and charge balance in the structure. As shown in the upper part of Figure 1b, the bond length of the Zn-Cl bond was between 2.271 Å and 2.297 Å in each  $[ZnCl_4]^{2-}$  tetrahedron. The bond length range of the Zn-Cl bond in the  $[ZnCl_4]^{2-}$  tetrahedron changed to 2.274 Å~2.323 Å after  $Zr^{4+}$  ions were introduced into the lattice of  $Cs_2ZnCl_4$ . Compared with undoped  $Cs_2ZnCl_4$ , the introduction of  $Zr^{4+}$  ions significantly increased the bond length of the Zn-Cl bond, which showed that the tetrahedral distortion in the doped system was greater than the undoped system. In addition, the bond angles of the four Cl-Zn-Cl also changed significantly after  $Zr^{4+}$  doping. In the undoped system, the bond angles of Cl1-Zn-Cl2, Cl2-Zn-Cl3, Cl3-Zn-Cl4, and Cl1-Zn-Cl4 were 106.479°, 109.046°, 109.636°, and 115.361°, respectively. After the introduction of Zr ions, the Cl1-Zn-Cl2 and Cl1-Zn-Cl4 bond angles decreased, while the Cl2-Zn-Cl3 and Cl3-Zn-Cl4 bond angles increased, as shown in the lower part of Figure 1b. The significant structural differences between the undoped system and the doped system also provide evidence that  $Zr^{4+}$  ions replaced a small part of the  $Zn^{2+}$  ions lattice. At the same time, this significant difference also showed the stronger distortion of the crystal lattice after  $Zr^{4+}$  doping, and easily generated the strong electron-phonon coupling effects under excitation, which is an intrinsic condition for efficient light emission [27–29].

The powder x-ray diffraction (PXRD) patterns of  $Cs_2ZnCl_4$  crystal samples at different  $Zr^{2+}$  doping concentrations are shown in Figure 1c. Each pattern was in good agreement with the standard diffraction pattern of  $Cs_2ZnCl_4$  (ICSD-6062) and no redundant impurity diffraction peaks appeared. This result shows that all samples were successfully synthesized and no impurity phase was produced. The uniformity of these patterns also confirms that the doping of  $Zr^{4+}$  did not change the original crystal structure of the  $Cs_2ZnCl_4$  host material. At the same time, the diffraction pattern of the sample showed a tendency to move to a lower angle as the  $Zr^{4+}$  feed ratio continued to increase, which confirms the successful doping of  $Zr^{4+}$  ions. Because larger  $Zr^{2+}$  ions (ionic radius: 0.6 Å for  $Zn^{2+}$  and 0.72 Å for  $Zr^{4+}$ ) were incorporated into the  $Cs_2ZnCl_4$  lattice, the lattice expanded, leading to the movement of the XRD diffraction peak to a lower angle [30,31]. The elemental composition of 20% $Zr^{4+}:Cs_2ZnCl_4$  was strictly characterized qualitatively and quantitatively. Energy spectroscopy (EDS) elemental mapping of the  $Zr^{4+}:Cs_2ZnCl_4$  crystal showed that Cs, Zn, Cl, and Zr elements were uniformly distributed (Figure S1a), indicating that  $Zr^{4+}$  ions were uniformly doped in the  $Cs_2ZnCl_4$  lattice, with a high phase purity. The measurement results showed that the atomic ratio of Cs:Zn:Zr:Cl was 33.55:11.26:0.39:54.81 while the feed ratio of  $Zr^{4+}$  ions was 20% (Figure S1b). The results of the elemental analysis showed that when the feed ratio of the  $Zr^{4+}$  ions in the experiment was 20%, the actual atomic percentage entering the  $Cs_2ZnCl_4$  lattice was

only 3.35%. This may have been due to the larger radius and higher valence of  $Zr^{4+}$  ions, which could not easily replace the lattice position of  $Zn^{2+}$ .

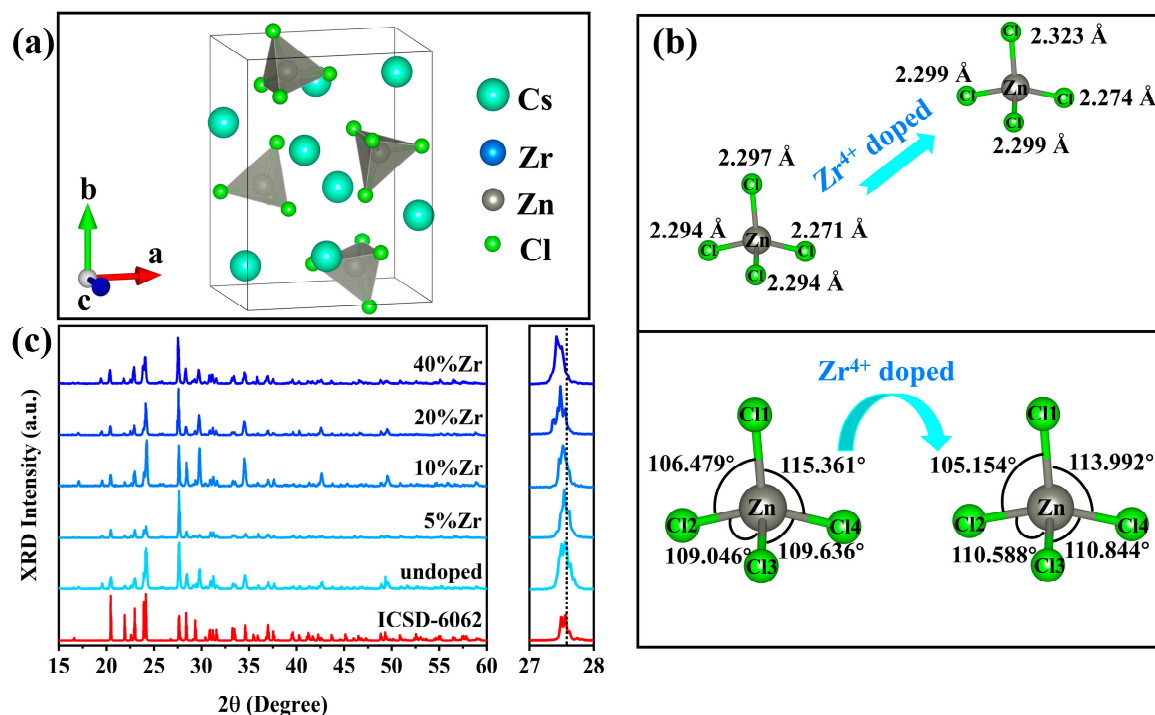
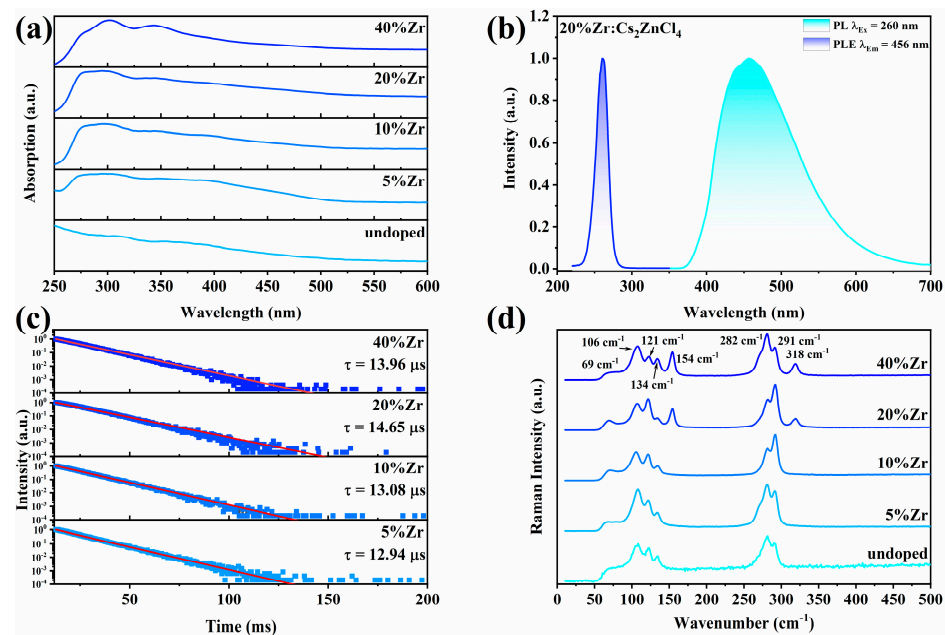


**Figure 1.** (a) The crystal structure of  $Cs_2ZnCl_4$ . (b) The bond length of Zn-Cl and the bond angle of Cl-Zn-Cl in a  $[ZnCl_4]^{2-}$  tetrahedron before and after  $Zr^{4+}$  doping. (c) The XRD patterns of  $Cs_2ZnCl_4$  with different  $Zr^{4+}$  feed ratios.

## 2.2. Optical Properties

In order to study the optical properties of  $Zr^{4+}:Cs_2ZnCl_4$ , the absorption spectra of  $Cs_2ZnCl_4$  at different  $Zr^{4+}$  doping ratios were first collected, as shown in Figure 2a. The absorption spectrum of the undoped sample showed that absorption intensity increased slowly as the wavelength decreased and no obvious absorption band appeared in the range from 250 nm to 600 nm. With the introduction of  $Zr^{4+}$  ions, two new absorption bands appeared at 300 nm and 350 nm. The intensity of these two absorption bands increased with the increase in the  $Zr^{4+}$  ion doping ratio. There is no doubt that the optical transition process corresponding to these two absorption bands was related to the exciton characteristics generated by structural distortion, which originated from the incorporation of  $Zr^{4+}$  ions [32–34].

Under the excitation of 260 nm UV light,  $Zr^{4+}:Cs_2ZnCl_4$  exhibited bright broadband blue emission in the range of 370 nm to 700 nm with a PL peak position at 456 nm, Stokes shift of 197 nm, and a full-width half maximum (FWHM) of 119.86 nm. The CIE coordinates of  $Zr^{4+}:Cs_2ZnCl_4$  and the optical photograph of the sample under 254 nm UV excitation are shown in Figure S2a. The PL intensity changed significantly due to the concentration quenching effect, showing an increase first and then a downward trend with the increase in the feeding ratios of  $Zr^{4+}$  (Figure S2b). When the  $Zr^{4+}$  feeding ratio was 20%, the PL intensity reached the maximum. In order to investigate the potential photophysical mechanism of these  $Zr^{4+}$  doped samples, the PLE spectra of  $Zr^{4+}:Cs_2ZnCl_4$  at different emission wavelengths and the PL spectra at different excitation wavelengths were collected. Figure S3a shows that the PLE spectra at different emission wavelengths all had similar profiles, which excluded the possibility that the blue emission came from other defects or impurities in the crystal. Figure S3b shows that the PL spectra of the samples obtained with different excitation wavelengths also had the same shape, indicating that this blue emission came from the same excited state relaxation.



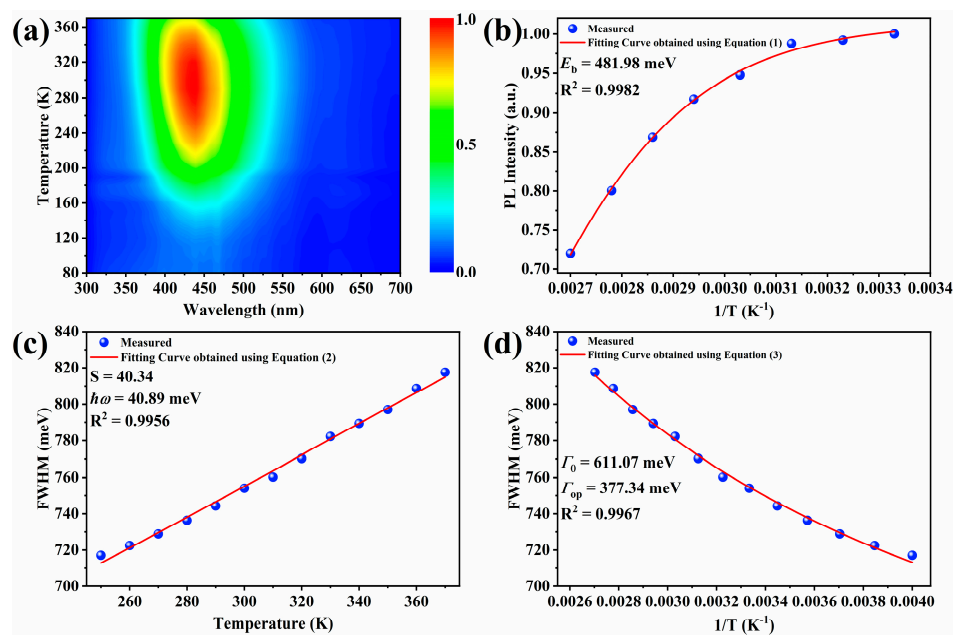
**Figure 2.** (a) Absorption spectra of Cs<sub>2</sub>ZnCl<sub>4</sub> with different Zr<sup>4+</sup> feed ratios. (b) Normalized PLE (with the monitoring wavelength at 457 nm) and PL (under the excitation wavelength at 260 nm) spectra of 20%Zr<sup>4+</sup>:Cs<sub>2</sub>ZnCl<sub>4</sub>. (c) PL lifetime of Cs<sub>2</sub>ZnCl<sub>4</sub> with different Zr<sup>4+</sup> feed ratios monitored at 260 nm. (d) Raman spectra of Cs<sub>2</sub>ZnCl<sub>4</sub> with different Zr<sup>4+</sup> feed ratios under the excitation of a 633 nm laser.

Figure 2c shows the PL lifetime decay curve of Cs<sub>2</sub>ZnCl<sub>4</sub> under different Zr<sup>4+</sup> doping ratios. The lifetime curves of all samples could be fitted using single exponential decay. All these samples exhibited decay lifetimes in the microsecond range. PL decay lifetime in the order of microseconds is a typical feature of STE emission, and the lifetime of this emission is usually longer than the lifetime of band-edge free excitons [27,35]. As the Zr<sup>4+</sup> doping amount gradually increased, the PL lifetime of these samples showed a trend of first increasing and then decreasing, with the longest lifetime at 20% doping amount, which was similar to the change trend of the PL spectrum (Figure S2b). The decrease in lifetime at high doping ratios was due to the concentration quenching effect of high concentrations of Zr<sup>4+</sup> ions because high concentrations of Zr<sup>4+</sup> ions will generate more non-radiative recombination paths to quench the emission. Characteristics such as broadband emission and long lifetime in the order of microseconds indicated that the bright blue emission in Zr<sup>4+</sup>:Cs<sub>2</sub>ZnCl<sub>4</sub> came from STE emission caused by strong electron–phonon coupling inside the crystal lattice. This strong electron–phonon coupling effect exists widely in “soft” lattice materials with less structural rigidity [35,36]. The strong electron–phonon coupling effect will cause elastic deformation of the lattice in this “soft” lattice structure, thereby binding the photogenerated excitons to certain specific positions on the lattice to form STEs. This state has a lower energy level than other excited states and, therefore, can exist stably. These excitons are bound to specific positions in the crystal lattice, and can only radiate photons outward through radiative recombination to produce emission. In addition, the sample obtained a high PLQY of 89.67% under 260 nm ultraviolet light excitation when the Zr<sup>4+</sup> ion doping amount was 20%. This indicates that Zr<sup>4+</sup>:Cs<sub>2</sub>ZnCl<sub>4</sub> has certain applications in the field of solid-state lighting and display (Figure S4).

In order to explore the electron–phonon coupling effect inside the sample, a 633 nm continuous laser was used as the excitation source to collect the Raman spectra of Cs<sub>2</sub>ZnCl<sub>4</sub> under different Zr<sup>2+</sup> doping ratios, as shown in Figure 2d. In all samples, six Raman peaks could be observed in the low wavenumber region (<500 cm<sup>-1</sup>). These were located at 69 cm<sup>-1</sup>, 106 cm<sup>-1</sup>, 121 cm<sup>-1</sup>, 134 cm<sup>-1</sup>, 282 cm<sup>-1</sup>, and 291 cm<sup>-1</sup>, respectively. In addition, new Raman peaks appeared near 154 cm<sup>-1</sup> and 318 cm<sup>-1</sup> when the Zr<sup>4+</sup> feed ratios were

20% and 40%, which may have been caused by high-concentration  $\text{Zr}^{4+}$  doping. It is worth noting that the Raman peak at  $282\text{ cm}^{-1}$  was the double frequency mode of the  $134\text{ cm}^{-1}$  Raman peak. This double frequency mode indicated that there was a strong electron–phonon coupling in  $\text{Zr}^{4+}:\text{Cs}_2\text{ZnCl}_4$ , which was very conducive to the formation of STE [37]. This result further proves that the broadband blue emission of  $\text{Zr}^{4+}:\text{Cs}_2\text{ZnCl}_4$  was a typical STE emission, which came from the strong electron–phonon coupling effect caused by the structure distortion.

To further explore the intrinsic photophysical properties in  $\text{Zr}^{4+}:\text{Cs}_2\text{ZnCl}_4$ , the temperature-dependent PL spectrum of  $\text{Zr}^{4+}:\text{Cs}_2\text{ZnCl}_4$  was measured. Figure 3a shows the map of the PL intensity of  $\text{Zr}^{4+}:\text{Cs}_2\text{ZnCl}_4$  plotted with temperature  $T$  and emission wavelength  $\lambda$  at the temperature range of 80–360 K under 260 nm UV excitation. The color scale represents the PL intensity, and the color change from blue to red represents the enhancement of the PL intensity from the minimum to the maximum at the temperature range of 80 K–300 K.  $\text{Zr}^{4+}:\text{Cs}_2\text{ZnCl}_4$  exhibited a single emission band ( $\lambda_{\text{em}} = 456\text{ nm}$ ) at all temperatures and additional emission bands appeared with temperature changes. In the temperature range of 80 K–150 K, the PL intensity of  $\text{Zr}^{4+}:\text{Cs}_4\text{ZnCl}_4$  was too weak to show the obvious emission signal. When the temperature was higher than 150 K, the PL intensity of  $\text{Zr}^{4+}:\text{Cs}_4\text{ZnCl}_4$  began to increase significantly with the increase in temperature and was strongest at 300 K. As the temperature increased further, PL intensity of  $\text{Zr}^{4+}:\text{Cs}_4\text{ZnCl}_4$  weakened. According to previous research, the formation of STEs requires the participation of a certain intensity of lattice vibration [27,32,35]. In  $\text{Zr}^{4+}:\text{Cs}_2\text{ZnCl}_4$ , the lattice vibration intensity required to generate STEs was stronger. The number of STEs formed was limited and effective emission could not be produced, due to the lattice vibration being significantly suppressed at low temperatures. The enhanced lattice vibration intensity promoted the formation of STEs when the temperature gradually increased, resulting in enhanced PL intensity. Finally, the promotion effect of lattice vibration on emission reached the maximum at 300 K, and the PL intensity was the highest. With further temperature increase, the strong lattice vibration will no longer promote emission but will produce a quenching effect. Therefore, the PL intensity of  $\text{Zr}^{4+}:\text{Cs}_2\text{ZnCl}_4$  began to decrease when the temperature was higher than 300 K.



**Figure 3.** (a) The map of the PL intensity of  $\text{Zr}^{4+}:\text{Cs}_2\text{ZnCl}_4$  plotted with temperature  $T$  and emission wavelength  $\lambda$  at the temperature range of 80–360 K. (b) Fitting results of exciton binding energy  $E_b$ . (c) Fitting results of Huang–Rhys factor  $S$ . (d) Fitting results of electron–optical-phonon coupling energy.

In addition, several key physical parameters, such as the Huang–Rhys factor ( $S$ ), the exciton binding energy ( $E_b$ ), and the electron–optical-phonon coupling energy ( $\Gamma_{op}$ ) were obtained by fitting the temperature-dependent PL spectrum. These physical parameters help to understand the underlying photophysical mechanism in  $Zr^{4+}:Cs_2ZnCl_4$ . First, the exciton binding energy of the  $Zr^{4+}:Cs_2ZnCl_4$  was fitted using the following formula [38]:

$$I(T) = \frac{I_0}{\left(1 + Ae^{\frac{-E_b}{k_b T}}\right)} \quad (1)$$

where  $I_0$  is the PL intensity at 0 K,  $I(T)$  is the PL intensity at temperature  $T$  K,  $k_b$  is the Boltzmann constant, and  $A$  is a constant. The fitting results, as given in Figure 3b, showed that the  $E_b$  of the  $Zr^{4+}:Cs_2ZnCl_4$  was 481.98 meV. Such a large exciton binding energy indicated that these STEs required high energy to generate, which was consistent with the optical behavior at different temperatures. At the same time, the larger the exciton binding energy, the more stable the photogenerated excitons and the higher the dissociation temperature, thereby ensuring that the emission had excellent thermal stability and resistance to thermal quenching.

The Huang–Rhys factor ( $S$ ) of the sample was obtained to investigate the electron–phonon coupling effect by fitting using the following formula [39]:

$$FWHM(T) = 2.36\sqrt{S}\hbar\omega_{\text{phonon}}\sqrt{\coth\frac{\hbar\omega_{\text{phonon}}}{2k_b T}} \quad (2)$$

where  $\omega_{\text{phonon}}$  is the phonon frequency,  $T$  is the temperature, FWHM is the full-width half maximum of the PL spectra, and  $k_b$  is the Boltzmann constant. The fitting results are shown in Figure 3c. The Huang–Rhys factor  $S$  of 40.34 meant that  $Zr^{4+}:Cs_2ZnCl_4$  had strong electron–phonon coupling. At the same time, the phonon energy  $\hbar\omega_{\text{phonon}}$  obtained by fitting was 40.89 meV, which was very close to the vibration energy of the  $291\text{ cm}^{-1}$  Raman peak in the Raman spectrum ( $\sim 36.08$  meV). This indicates that the  $291\text{ cm}^{-1}$  Raman peak mainly participated in the formation of STEs in  $Zr^{4+}:Cs_2ZnCl_4$ . The large  $S$  value, broadband emission, and large Stokes shift (197 nm) indicated that the blue emission of  $Zr^{4+}:Cs_2ZnCl_4$  originated from self-trapped excitons generated by strong Jahn–Teller distortion. The Toyokawa equation was used to fit the change in PL spectrum FWHM with temperature to further investigate the electron–phonon coupling effect in the  $Zr^{4+}:Cs_2ZnCl_4$  [40]:

$$\Gamma(T) = \Gamma_0 + \frac{\Gamma_{op}}{e^{\frac{\hbar\omega_{op}}{k_b T}} - 1} \quad (3)$$

where  $\Gamma_0$  is the FWHM of PL spectra at 0 K,  $\Gamma_{op}$  is the electron–optical-phonon coupling energy,  $\hbar\omega_{op}$  is the energy of long optical phono, and  $k_b$  is the Boltzmann constant.  $\hbar\omega_{op}$  was obtained by fitting the Huang–Rhys factor  $S$ , which was 40.89. As shown in Figure 3d, the fitted  $\Gamma_0$  and  $\Gamma_{op}$  were 611.07 meV and 377.34 meV, respectively. Such a large electron–optical-phonon coupling energy  $\Gamma_0$  indicates that there was a strong electron–phonon coupling in the  $Zr^{4+}:Cs_2ZnCl_4$  structure, which had a crucial impact on the generation of STEs.

### 2.3. Theoretical Calculation and Photophysical Model

In order to explore the electronic structure of  $Zr^{4+}:Cs_2ZnCl_4$  and the intrinsic physical mechanism of efficient blue emission, the bandgap structure and density of state (DOS) of  $Cs_2ZnCl_4$  and  $Zr^{4+}:Cs_2ZnCl_4$  were calculated using first principles. Figure 4a,c show the bandgap structures of  $Cs_2ZnCl_4$  and  $Zr^{4+}:Cs_2ZnCl_4$ , respectively. Interestingly, the band edge after doping with  $Zr^{4+}$  ions was flatter than that of pure  $Cs_2ZnCl_4$ , which means that the doping of  $Zr^{4+}$  ions enhanced the quantum confinement effect because the flat conduction band and valence band meant small dispersion and large carrier effective mass,

which is a typical feature of a strong quantum confinement effect [41]. The strong quantum confinement effect was very important for the highly localized exciton formation. Once excitons were formed under excitation, they would be confined to isolated inorganic polyhedrons due to the unique quantum confinement effect of the zero-dimensional structure. There was no interaction due to the large distance between adjacent polyhedrons, leading to highly efficient luminescence in  $\text{Zr}^{4+}:\text{Cs}_2\text{ZnCl}_4$ . Figure 4b,d show the DOS of  $\text{Cs}_2\text{ZnCl}_4$  and  $\text{Zr}^{4+}:\text{Cs}_2\text{ZnCl}_4$ , respectively. As shown in Figure 4b, the valence band maximum (VBM) of  $\text{Cs}_2\text{ZnCl}_4$  was mainly composed of Zn-3d and Cl-3p orbitals, while Zn-4s, Cl-3p, and Cl-3s orbitals together constituted the conduction band minimum (CBM). The VBM of  $\text{Zr}^{4+}:\text{Cs}_2\text{ZnCl}_4$  was mainly composed of Zn-3d and Cl-3p orbitals, while the Cl-3p and Zr-4d orbitals together constituted the CBM of  $\text{Zr}^{4+}:\text{Cs}_2\text{ZnCl}_4$  (Figure 4d). In addition, we also calculated the 3D and 2D electron distribution maps of VBM and CBM in the two compounds, as shown in Figure S5. Through the 3D and 2D electron distribution diagrams of VBM and CBM in pure ((a)–(d))  $\text{Cs}_2\text{ZnCl}_4$  and ((e)–(h))  $\text{Zr}^{4+}:\text{Cs}_2\text{ZnCl}_4$ , we can intuitively see that the VBM of  $\text{Cs}_2\text{ZnCl}_4$  was mainly composed of Zn and Cl orbitals, while Zn and Cl orbitals together constituted the CBM. The VBM of  $\text{Zr}^{4+}:\text{Cs}_2\text{ZnCl}_4$  was mainly composed of Zn and Cl orbitals, while the Zr orbitals constituted the CBM of  $\text{Zr}^{4+}:\text{Cs}_2\text{ZnCl}_4$ . The DOS of  $\text{Zr}^{4+}:\text{Cs}_2\text{ZnCl}_4$  showed that its bright blue emission was related to the doping of  $\text{Zr}^{4+}$  ions. Combining the PL spectrum and PL decay lifetime, it can be further confirmed that this blue emission originated from self-trapped excitons generated by lattice distortion caused by  $\text{Zr}^{4+}$  ion doping. The ultra-high PLQY of close to 100% in  $\text{Zr}^{4+}:\text{Cs}_2\text{ZnCl}_4$  could be assigned to the highly localized exciton distribution in the structure, which benefited from the strong quantum confinement effect unique to the zero-dimensional structure.

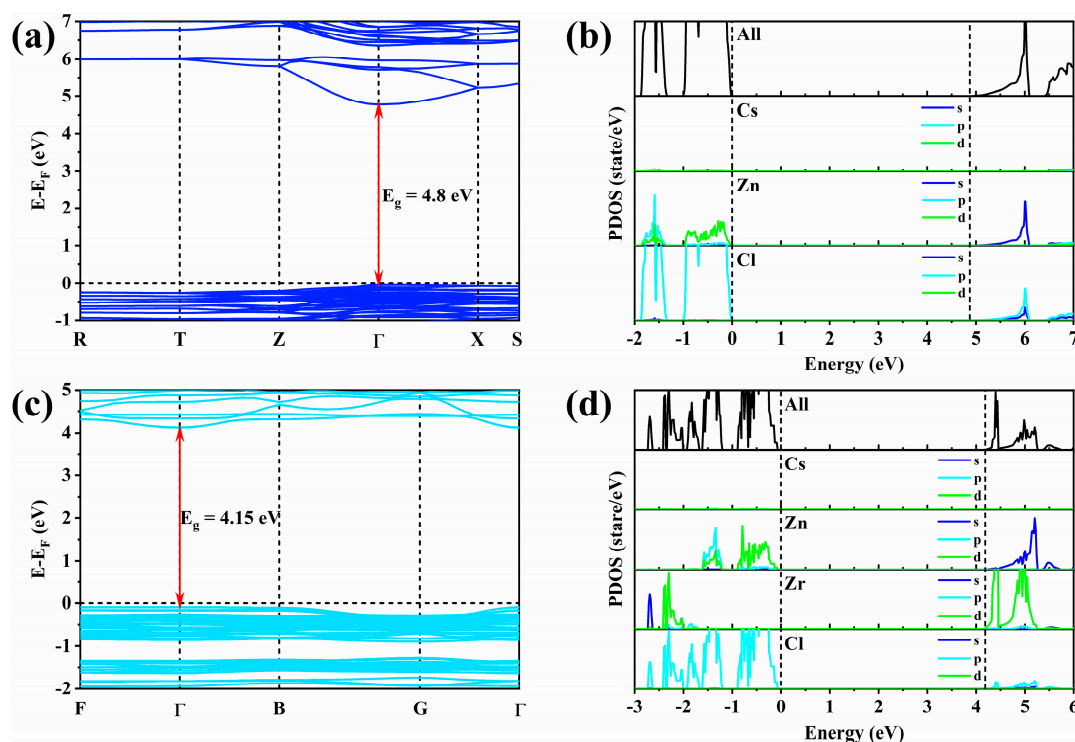


**Figure 4.** (a) Bandgap structure of undoped  $\text{Cs}_2\text{ZnCl}_4$ . (b) DOS of undoped  $\text{Cs}_2\text{ZnCl}_4$ . (c) Bandgap structure of  $\text{Zr}^{4+}:\text{Cs}_2\text{ZnCl}_4$ . (d) DOS of  $\text{Zr}^{4+}:\text{Cs}_2\text{ZnCl}_4$ .

As shown in Figure 5, ground state electrons absorbed energy and transitioned to the excited state under UV excitation. Due to the soft lattice properties of  $\text{Zr}^{4+}:\text{Cs}_2\text{ZnCl}_4$ , the lattice deformed rapidly after being excited and bound the excited electrons to specific sites in the lattice. The bound electrons then radiated photons outward through radiative recombination and produced bright blue-light emission.

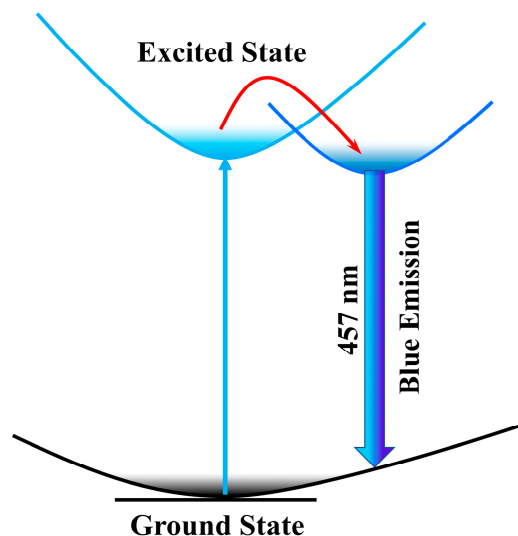


**Figure 5.** Schematic diagram of the photophysical model of  $\text{Zr}^{4+}:\text{Cs}_2\text{ZnCl}_4$ .

### 3. Conclusions

In summary, in this work, we report an all-inorganic zero-dimensional metal halide  $\text{Zr}^{4+}:\text{Cs}_2\text{ZnCl}_4$  with efficient broadband blue emission. Under the excitation of 260 nm UV light,  $\text{Zr}^{4+}:\text{Cs}_2\text{ZnCl}_4$  exhibited broadband blue emission at 457 nm, with a PLQY of up to 89.67%. Combining the room- and low-temperature PL spectra with the PL decay lifetime, confirmed that the broadband blue emission in  $\text{Zr}^{4+}:\text{Cs}_2\text{ZnCl}_4$  came from self-trapped excitons generated by structural distortion after  $\text{Zr}^{4+}$  ion doping. First-principles calculation results showed that the efficient emission came from the strong quantum confinement effect generated by the unique zero-dimensional structure of  $\text{Cs}_2\text{ZnCl}_4$ . We believe this work can provide a reference for the future design and synthesis of low-dimensional metal halide materials with high luminescence efficiency.

**Supplementary Materials:** The following supporting information can be downloaded at: <https://www.mdpi.com/article/10.3390/molecules29071651/s1>, Experimental and computational details and supplementary figures (PDF). Ref. [42] is cited in Supplementary Materials.

**Author Contributions:** Conceptualization, Y.T. and C.P.; methodology, Y.T.; software, Q.W.; Resources, L.D.; writing—original draft preparation, Y.T. and C.P.; writing—review and editing, Y.T. All authors have read and agreed to the published version of the manuscript.

**Funding:** This work was financially supported by the National Natural Science Foundation of China (Grant No. 62175219), the Fundamental Research Program of Shanxi Province (Grant No. 20210302124397) and the Open Research Fund of the State Key Laboratory of Dynamic Testing (Technology Grant No. 2022-SYSJJ-01).

**Data Availability Statement:** Data are contained within the article and Supplementary Materials.

**Conflicts of Interest:** The authors declare no conflicts of interest.

### References

1. Ponce, F.; Bour, D. Nitride-Based Semiconductors for Blue and Green Light-Emitting Devices. *Nature* **1997**, *386*, 351–359. [\[CrossRef\]](#)
2. Fasol, G.; Nakamura, S. *The Blue Laser Diode*; Springer-Verlag: Berlin/Heidelberg, Germany, 1997.
3. Zhou, C.; Lin, H.; He, Q.; Xu, L.; Worku, M.; Chaaban, M.; Lee, S.; Shi, X.; Du, M.-H.; Ma, B. Low Dimensional Metal Halide Perovskites and Hybrids. *Mater. Sci. Eng. R* **2019**, *137*, 38–65. [\[CrossRef\]](#)
4. Jiang, T.; Ma, W.; Zhang, H.; Tian, Y.; Lin, G.; Xiao, W.; Yu, X.; Qiu, J.; Xu, X.; Yang, Y. Highly Efficient and Tunable emission of Lead-Free Manganese Halides toward White Light-Emitting Diode and X-ray Scintillation Applications. *Adv. Funct. Mater.* **2021**, *31*, 2009973. [\[CrossRef\]](#)
5. Han, P.; Luo, C.; Yang, S.; Yang, Y.; Deng, W.; Han, K. All-Inorganic Lead-Free 0D Perovskites by A Doping Strategy to Achieve A PLQY Boost from <2% to 90%. *Angew. Chem. Int. Ed.* **2020**, *132*, 12809–12813.

6. Li, Z.; Li, Y.; Liang, P.; Zhou, T.; Wang, L.; Xie, R.-J. Dual-Band Luminescent Lead-Free Antimony Chloride Halides with Near-Unity Photoluminescence Quantum Efficiency. *Chem. Mater.* **2019**, *31*, 9363–9371. [[CrossRef](#)]
7. Zhou, C.; Lin, H.; Tian, Y.; Yuan, Z.; Clark, R.; Chen, B.; van de Burgt, L.J.; Wang, J.C.; Zhou, Y.; Hanson, K. Luminescent Zero-Dimensional Organic Metal Halide Hybrids with Near-Unity Quantum Efficiency. *Chem. Sci.* **2018**, *9*, 586–593. [[CrossRef](#)] [[PubMed](#)]
8. Zhou, C.; Lin, H.; Shi, H.; Tian, Y.; Pak, C.; Shatruk, M.; Zhou, Y.; Djurovich, P.; Du, M.H.; Ma, B. A Zero-Dimensional Organic Seesaw-Shaped Tin Bromide with Highly Efficient Strongly Stokes-Shifted Deep-Red Emission. *Angew. Chem. Int. Ed.* **2018**, *130*, 1033–1036. [[CrossRef](#)]
9. Zhou, C.; Worku, M.; Neu, J.; Lin, H.; Tian, Y.; Lee, S.; Zhou, Y.; Han, D.; Chen, S.; Hao, A. Facile Preparation of Light Emitting Organic Metal Halide Crystals with Near-Unity Quantum Efficiency. *Chem. Mater.* **2018**, *30*, 2374–2378. [[CrossRef](#)]
10. Zhou, L.; Liao, J.F.; Huang, Z.G.; Wei, J.H.; Wang, X.D.; Li, W.G.; Chen, H.Y.; Kuang, D.B.; Su, C.Y. A Highly Red-Emissive Lead-Free Indium-Based Perovskite Single Crystal for Sensitive Water Detection. *Angew. Chem. Int. Ed.* **2019**, *131*, 5331–5335. [[CrossRef](#)]
11. Morad, V.; Shynkarenko, Y.; Yakunin, S.; Brumberg, A.; Schaller, R.D.; Kovalenko, M.V. Disphenoidal Zero-Dimensional Lead, Tin, and Germanium Halides: Highly Emissive Singlet and Triplet Self-Trapped Excitons and X-ray Scintillation. *J. Am. Chem. Soc.* **2019**, *141*, 9764–9768. [[CrossRef](#)]
12. Lin, H.; Zhou, C.; Chaaban, M.; Xu, L.-J.; Zhou, Y.; Neu, J.; Worku, M.; Berkwits, E.; He, Q.; Lee, S. Bulk Assembly of Zero-Dimensional Organic Lead Bromide Hybrid with Efficient Blue Emission. *ACS Mater. Lett.* **2019**, *1*, 594–598. [[CrossRef](#)]
13. Zhou, C.; Lin, H.; Worku, M.; Neu, J.; Zhou, Y.; Tian, Y.; Lee, S.; Djurovich, P.; Siegrist, T.; Ma, B. Blue Emitting Single Crystalline Assembly of Metal Halide Clusters. *J. Am. Chem. Soc.* **2018**, *140*, 13181–13184. [[CrossRef](#)]
14. Jun, T.; Sim, K.; Iimura, S.; Sasase, M.; Kamioka, H.; Kim, J.; Hosono, H. Lead-Free Highly Efficient Blue-Emitting Cs<sub>3</sub>Cu<sub>2</sub>I<sub>5</sub> with 0D Electronic Structure. *Adv. Mater.* **2018**, *30*, 1804547. [[CrossRef](#)] [[PubMed](#)]
15. Huang, J.; Su, B.; Song, E.; Molocheev, M.S.; Xia, Z. Ultra-Broad-Band-Excitable Cu(I)-Based Organometallic Halide with Near-Unity Emission for Light-Emitting Diode Applications. *Chem. Mater.* **2021**, *33*, 4382–4389. [[CrossRef](#)]
16. Creason, T.D.; Yangui, A.; Roccanova, R.; Strom, A.; Du, M.H.; Saparov, B. Rb<sub>2</sub>CuX<sub>3</sub> (X = Cl, Br): 1D All-Inorganic Copper Halides with Ultrabright Blue Emission and Up-Conversion Photoluminescence. *Adv. Opt. Mater.* **2020**, *8*, 1901338. [[CrossRef](#)]
17. Liu, X.; Yuan, F.; Zhu, C.; Li, J.; Lv, X.; Xing, G.; Wei, Q.; Wang, G.; Dai, J.; Dong, H. Near-Unity Blue Luminescence from Lead-Free Copper Halides for Light-Emitting Diodes. *Nano Energy* **2022**, *91*, 106664. [[CrossRef](#)]
18. Li, H.; Lv, Y.; Zhou, Z.; Tong, H.; Liu, W.; Ouyang, G. Coordinated Anionic Inorganic Module—An Efficient Approach towards Highly Efficient Blue-Emitting Copper Halide Ionic Hybrid Structures. *Angew. Chem. Int. Ed.* **2022**, *61*, e202115225. [[CrossRef](#)] [[PubMed](#)]
19. Song, G.; Li, M.; Yang, Y.; Liang, F.; Huang, Q.; Liu, X.; Gong, P.; Xia, Z.; Lin, Z. Lead-Free Tin (IV)-Based Organic–Inorganic Metal Halide Hybrids with Excellent Stability and Blue-Broadband Emission. *J. Phys. Chem. Lett.* **2020**, *11*, 1808–1813. [[CrossRef](#)] [[PubMed](#)]
20. Fattal, H.; Creason, T.D.; Delzer, C.J.; Yangui, A.; Hayward, J.P.; Ross, B.J.; Du, M.-H.; Glatzhofer, D.T.; Saparov, B. Zero-Dimensional Hybrid Organic–Inorganic Indium Bromide with Blue Emission. *Inorg. Chem.* **2021**, *60*, 1045–1054. [[CrossRef](#)]
21. Ma, Y.-Y.; Fu, H.-Q.; Liu, X.-L.; Sun, Y.-M.; Zhong, Q.-Q.; Xu, W.-J.; Lei, X.-W.; Liu, G.-D.; Yue, C.-Y. Zero-Dimensional Organic–Inorganic Hybrid Indium Chlorides with Intrinsic Blue Light Emissions. *Inorg. Chem.* **2022**, *61*, 8977–8981. [[CrossRef](#)]
22. Li, D.-Y.; Sun, Y.-M.; Wang, X.-Y.; Wang, N.-N.; Zhang, X.-Y.; Yue, C.-Y.; Lei, X.-W. Zero-Dimensional Hybrid Indium Halides with Efficient and Tunable White-Light Emissions. *J. Phys. Chem. Lett.* **2022**, *13*, 6635–6643. [[CrossRef](#)] [[PubMed](#)]
23. Babu, R.; López-Fernández, I.; Prasanthkumar, S.; Polavarapu, L. All-Inorganic Lead-Free Doped-Metal Halides for Bright Solid-State Emission from Primary Colors to White Light. *ACS Appl. Mater. Interfaces* **2023**, *15*, 35206–35215. [[CrossRef](#)]
24. Yang, Y.; Wu, J.; Zhou, T.; Wang, Y.; Zheng, J.; Liu, R.; Hou, J.; Li, X.; Wang, L.; Jiang, W. Efficient Emission in Copper-Doped Cs<sub>3</sub>ZnX<sub>5</sub> (X = Cl, I) for White LEDs and X-ray Scintillators. *J. Mater. Chem. C* **2023**, *11*, 9850–9859. [[CrossRef](#)]
25. Tang, Y.; Deng, M.; Zhou, Z.; Kang, C.; Wang, J.; Liu, Q. Recent Advances in Lead-Free Cs<sub>2</sub>ZrCl<sub>6</sub> Metal Halide Perovskites and Their Derivatives: From Fundamentals to Advanced Applications. *Coord. Chem. Rev.* **2024**, *499*, 215490. [[CrossRef](#)]
26. He, Y.; Liu, S.; Yao, Z.; Zhao, Q.; Chabera, P.; Zheng, K.; Yang, B.; Pullerits, T.; Chen, J. Nature of Self-Trapped Exciton Emission in Zero-Dimensional Cs<sub>2</sub>ZrCl<sub>6</sub> Perovskite Nanocrystals. *J. Phys. Chem. Lett.* **2023**, *14*, 7665–7671. [[CrossRef](#)] [[PubMed](#)]
27. Dohner, E.R.; Hoke, E.T.; Karunadasa, H.I. Self-Assembly of Broadband White-Light Emitters. *J. Am. Chem. Soc.* **2014**, *136*, 1718–1721. [[CrossRef](#)]
28. Mao, L.; Wu, Y.; Stoumpos, C.C.; Wasielewski, M.R.; Kanatzidis, M.G. White-Light Emission and Structural Distortion in New Corrugated Two-Dimensional Lead Bromide Perovskites. *J. Am. Chem. Soc.* **2017**, *139*, 5210–5215. [[CrossRef](#)]
29. Peng, C.; Zhuang, Z.; Yang, H.; Zhang, G.; Fei, H. Ultrastable, Cationic Three-Dimensional Lead Bromide Frameworks that Intrinsically Emit Broadband White-Light. *Chem. Sci.* **2018**, *9*, 1627–1633. [[CrossRef](#)]
30. Cheng, P.; Feng, L.; Liu, Y.; Zheng, D.; Sang, Y.; Zhao, W.; Yang, Y.; Yang, S.; Wei, D.; Wang, G. Doped Zero-Dimensional Cesium Zinc Halides for High-Efficiency Blue Light Emission. *Angew. Chem. Int. Ed.* **2020**, *59*, 21414–21418. [[CrossRef](#)]
31. Wang, J.; Yu, Y.; Li, S.; Guo, L.; Wang, E.; Cao, Y. Doping Behavior of Zr<sup>4+</sup> Ions in Zr<sup>4+</sup>-Doped TiO<sub>2</sub> Nanoparticles. *J. Phys. Chem. C* **2013**, *117*, 27120–27126. [[CrossRef](#)]

32. Dohner, E.R.; Jaffe, A.; Bradshaw, L.R.; Karunadasa, H.I. Intrinsic White-Light Emission from Layered Hybrid Perovskites. *J. Am. Chem. Soc.* **2014**, *136*, 13154–13157. [[CrossRef](#)]
33. Cortecchia, D.; Yin, J.; Bruno, A.; Lo, S.-Z.A.; Gurzadyan, G.G.; Mhaisalkar, S.; Brédas, J.-L.; Soci, C. Polaron Self-Localization in White-Light Emitting Hybrid Perovskites. *J. Mater. Chem. C* **2017**, *5*, 2771–2780. [[CrossRef](#)]
34. Liu, X.; Peng, C.; Zhang, L.; Guo, D.; Pan, Y. Te<sup>4+</sup>-Doped Zero-Dimensional Cs<sub>2</sub>ZnCl<sub>4</sub> Single Crystals for Broadband Yellow Light Emission. *J. Mater. Chem. C* **2022**, *10*, 204–209. [[CrossRef](#)]
35. Li, S.; Luo, J.; Liu, J.; Tang, J. Self-Trapped Excitons in All-Inorganic Halide Perovskites: Fundamentals, Status, and Potential Applications. *J. Phys. Chem. Lett.* **2019**, *10*, 1999–2007. [[CrossRef](#)] [[PubMed](#)]
36. Zhou, L.; Liao, J.F.; Huang, Z.G.; Wei, J.H.; Wang, X.D.; Chen, H.Y.; Kuang, D.B. Intrinsic Self-Trapped Emission in 0D Lead-Free (C<sub>4</sub>H<sub>14</sub>N<sub>2</sub>)<sub>2</sub>In<sub>2</sub>Br<sub>10</sub> Single Crystal. *Angew. Chem. Int. Ed.* **2019**, *131*, 15581–15586. [[CrossRef](#)]
37. Peng, C.; Wei, Q.; Yao, S.; Meng, X.; Yu, Z.; Peng, H.; Zhong, X.; Zou, B. H<sub>2</sub>O–NH<sub>4</sub><sup>+</sup>-Induced Emission Modulation in Sb<sup>3+</sup>-Doped (NH<sub>4</sub>)<sub>2</sub>InCl<sub>5</sub>·H<sub>2</sub>O. *Inorg. Chem.* **2022**, *61*, 12406–12414. [[CrossRef](#)] [[PubMed](#)]
38. Yang, B.; Yin, L.; Niu, G.; Yuan, J.H.; Xue, K.H.; Tan, Z.; Miao, X.S.; Niu, M.; Du, X.; Song, H. Lead-Free Halide Rb<sub>2</sub>CuBr<sub>3</sub> as Sensitive X-ray Scintillator. *Adv. Mater.* **2019**, *31*, 1904711. [[CrossRef](#)] [[PubMed](#)]
39. Jing, Y.; Liu, Y.; Jiang, X.; Molokeev, M.S.; Lin, Z.; Xia, Z. Sb<sup>3+</sup> Dopant and Halogen Substitution Triggered Highly Efficient and Tunable Emission in Lead-Free Metal Halide Single Crystals. *Chem. Mater.* **2020**, *32*, 5327–5334. [[CrossRef](#)]
40. Gong, X.; Voznyy, O.; Jain, A.; Liu, W.; Sabatini, R.; Piontkowski, Z.; Walters, G.; Bappi, G.; Nokhrin, S.; Bushuyev, O. Electron–Phonon Interaction in Efficient Perovskite Blue Emitters. *Nat. Mater.* **2018**, *17*, 550–556. [[CrossRef](#)]
41. Li, Z.; Zhang, C.; Li, B.; Lin, C.; Li, Y.; Wang, L.; Xie, R.-J. Large-Scale Room-Temperature Synthesis of High-Efficiency Lead-Free Perovskite Derivative (NH<sub>4</sub>)<sub>2</sub>SnCl<sub>6</sub>:Te Phosphor for Warm wLEDs. *Chem. Eng. J.* **2021**, *420*, 129740. [[CrossRef](#)]
42. Giannozzi, P.; Baroni, S.; Bonini, N.; Calandra, M.; Car, R.; Cavazzoni, C.; Ceresoli, D.; Chiarotti, G.L.; Cococcioni, M.; Dabo, I. QUANTUM ESPRESSO: A modular and Ppen-Source Software Project for Quantum Simulations of Materials. *J. Phys. Condens. Matter* **2009**, *21*, 395502. [[CrossRef](#)] [[PubMed](#)]

**Disclaimer/Publisher’s Note:** The statements, opinions and data contained in all publications are solely those of the individual author(s) and contributor(s) and not of MDPI and/or the editor(s). MDPI and/or the editor(s) disclaim responsibility for any injury to people or property resulting from any ideas, methods, instructions or products referred to in the content.